RSC Advances

PAPER

View Article Online
View Journal | View Issue

Cite this: *RSC Adv.*, 2026, **16**, 10944

A portable paper-based and smartphone-assisted colorimetric sensor for copper oxychloride

Muhammad Adnan Sami,[a] Daim Asif Raja,[abc] Imdad Ali,[ae] Farid Ahmed,[d] Mahmood Fazal,[a] Muhammad Raza Shah *[a] and Muhammad Imran Malik *[ab]

Copper oxychloride (CuOxy) is a copper-containing fungicide and bactericide used to combat fungal diseases in fruits, vegetables, and ornamental crops. The maximum residue limit (MRL) for CuOxy is crop- and region-specific. The MRL for CuOxy is set in a range of 5–30 mg kg^{-1} for different sources by the European Food Safety Authority (EFSA). Herein, we report a novel colorimetric sensing platform based on coumarin triazole-functionalized silver nanoparticles (CT-AgNPs) for rapid, selective, and highly sensitive detection of CuOxy. The CT-AgNPs-based sensor exhibits excellent sensitivity, with a limit of detection (LoD) of 0.007 μM, a limit of quantification (LoQ) of 0.023 μM, and a linear detection range (LDR) of 0.1–100 μM. The system is efficiently integrated with AI-assisted smartphone detection and paper-based analytical devices (PADs) for real-time, on-site detection of CuOxy. Under optimized conditions, the sensor demonstrated outstanding selectivity, with no substantial interference from other environmental contaminants. The sensor's real-world applicability was verified through testing on actual samples, including tap and river water, along with different fruits and vegetables. To our knowledge, this is the first report of a CuOxy sensor combining both smartphone integration and paper-based analysis. The approach demonstrated high recovery rates in various environmental samples, validating its capability for quantitative CuOxy monitoring and offering a promising tool for ensuring food safety and environmental health.

Received 21st October 2025
Accepted 16th February 2026

DOI: 10.1039/d5ra08077k

rsc.li/rsc-advances

1 Introduction

Water is an important and crucial ingredient for life. More than 70% of the planet Earth is water, of which 68% is saline, and 3% is freshwater. Life on earth primarily depends on freshwater, which anthropogenic activities have polluted; the three most dominant contributors are human settlements, industries, and agriculture.[1–3] Many emerging pollutants, including antibiotics, cosmetics, and pesticides, are continuously polluting the freshwater reservoirs of the world. This increasing contamination renders the emergence of severe public health issues.[4,5]

Pesticides are one of the major classes of emerging pollutants classified as herbicides, rodenticides, and fungicides. As per a recent estimate, approximately 33% of crops are damaged by pests, having a direct impact on their yield.[6,7] Therefore, the use of pesticides is essential for improved production of cultivable crops. Thus, the annual worldwide use of pesticides has exceeded 3.5 million tons.[8] Due to excessive use, significant amounts of different pesticides are released into environmental compartments, such as soil and water. Typically, the pesticides detected in water are in low concentrations, *i.e.*, from low ng L^{-1} to a few μg L^{-1}. Nonetheless, these are still harmful to human life and aquatic organisms. Owing to the public health concern, government agencies offer guidelines regarding the minimization of the use of harmful pollutants, synthesizing less harmful pesticides, and decreasing maximum concentration limits of these pesticides in freshwater.[9–14] Thus, fast, robust, and economic analytical methodologies for quantitative detection of pesticides in real samples are highly sought-after.[15,16]

Copper oxychloride (CuOxy) is a copper-containing fungicide and bactericide used to combat fungal diseases in fruits, vegetables, and ornamental crops. The maximum residue limit (MRL) for CuOxy is crop- and region-specific. The MRL for CuOxy is set in a range of 5–30 mg kg^{-1} for different sources by the European Food Safety Authority (EFSA). For quantitative determination of CuOxy, various analytical methods have been reported such as flow injection chemiluminescence (FIA),[17] gas chromatography-mass spectrometry (GC-MS),[18] reverse phase high performance liquid chromatography with ultraviolet detection (RP-HPLC-UV),[19] liquid chromatography-mass spectrometry (LC-MS),[20] electrothermal atomic absorption spectroscopy (ETAAS),[21] liquid chromatography-mass spectrometry/

[a]*H.E.J. Research Institute of Chemistry, International Center for Chemical and Biological Sciences (ICCBS), University of Karachi, Karachi 75270, Pakistan. E-mail: raza.shah@iccs.edu; mimran.malik@iccs.edu*
[b]*Third World Center for Science and Technology, International Center for Chemical and Biological Sciences (ICCBS), University of Karachi, Karachi 75270, Pakistan*
[c]*School of Science, Minzu University of China, Beijing 100081, China*
[d]*Institute for Advanced Study, Shenzhen University, Shenzhen 518060, China*
[e]*Department of Chemistry, University of Selcuk, Konya, 42031, Turkey*

atomic absorption spectroscopy (LCMS/AAS),[22] and diffuse reflectance-near infrared spectroscopy (DIR-NIR).[22] However, most of these methods are associated with certain caveats, such as pre-treatment of the sample, requiring well-trained technicians, high cost, long protocols, low sensitivity, and limited selectivity. To overcome these limitations, the development of facile, fast, efficient, and accurate CuOxy detection methods in environmental samples is a challenging task. Such methods are needed for real-time, accurate, on-the-spot, and visual monitoring in the context of food safety and human health.[23–25]

With the rapid progress of nanotechnology, nanoparticles have been extensively explored for their diverse research applications and unique physicochemical attributes.[26–30] Metal nanoparticles (MNPs) are particularly important because they can undergo surface electron transitions from the valence band to the conduction band when interacting with electromagnetic radiation. This unique behavior confers them outstanding catalytic and optical properties, supporting their use in a broad range of applications, including catalysis and contaminant removal,[31] sensing,[17,32] and drug delivery.[33–42] Especially, silver (Ag) and gold (Au) nanoparticles (NPs) have drawn considerable interest in sensor technologies because of their distinctive optical characteristics. Their surface plasmon resonance (SPR) bands, typically observed between 200 and 750 nm, shift noticeably in response to external species, reflecting changes in the surrounding environment of NPs. Despite these advantages, metal nanoparticles face the challenge of rapid aggregation, which reduces their stability and functional performance. To counteract this issue, diverse capping agents are utilized, ranging from natural biomolecules such as proteins, polysaccharides, and flavonoids to synthetic stabilizers like organic molecules and polymers.[37,40,43–46] Silver nanoparticles stabilized with triazole moiety (ligands) have been widely used as a probe colorimetric sensor for the detection of heavy metal ions,[47,48] drugs, and pesticides.[49] Stabilized silver nanoparticles (AgNPs) are widely used in sensing applications, as their aggregation or stabilization is triggered by interactions between surface functional groups and the analyte, a process that largely depends on the type of stabilizing agent and the nature of the analyte.[3]

Developing on-the-spot assays for environmental contaminants like pesticides and drugs is a key challenge for analytical chemists. The combination of colorimetric assays and portable instruments has significantly advanced the real-time analysis. These assays indicate contaminant levels through color changes, enhanced by smartphones with high-resolution cameras and AI-inspired applications like color meter, which measure RGB values to correlate color intensity with concentration. Colorimetric assays can be converted into paper-based analytical devices (PADs), where color changes are analyzed with AI-inspired applications like ImageJ to determine grayscale values. Various assays, including enzyme assays, fluorescence-based chemical sensing, multimodal analysis, polymer and metal nanoparticle-based methods, facilitate the development of such on-the-spot sensors.[28,50–55]

In this context, coumarin-triazole-based ligands provide a highly versatile framework for the stabilization and functionalization of silver nanoparticles (AgNPs), while simultaneously enabling selective metal-ion detection.[56] The triazole moiety, enriched with multiple nitrogen donor atoms, exhibits strong affinity toward the AgNP surface, leading to enhanced nanoparticle stability, controlled growth, and long-term colloidal robustness.[57] Moreover, synergistic coordination between metal cations and triazole nitrogen atoms, together with coumarin-derived donor sites, facilitates regulated interparticle aggregation and modulates the surface electronic properties of AgNPs.[58]

In this study, we report the synthesis of coumarin triazole-based conjugated silver nanoparticles (CT-AgNPs) and their application as a sensing material. CT-AgNPs had a distinct pale yellow color and demonstrated a stable LSPR absorbance peak at 408 nm. Upon CuOxy introduction, the color of CT-AgNPs immediately turned light pink due to aggregation, accompanied by significant hypochromic and bathochromic shifts with a visible spectral broadening. This visual color change was seamlessly integrated with smartphone-asisted PADs for on-site detection of CuOxy. Furthermore, the CT-AgNPs were successfully applied for colorimetric, smartphone, and paper-based CuOxy detection in real environmental samples such as river and tap water, as well as food samples including guava, orange, turnip, and spinach. The developed CuOxy sensor demonstrated excellent sensitivity and selectivity for the on-site detection of CuOxy in environmental and agricultural samples, eliminating the need for a dedicated laboratory setup.

2 Experimental section

2.1 Materials and instrumentation

Vanillin, propargyl bromide, potassium carbonate, sodium azide, copper sulphate, sodium ascorbate, and ethyl 2-(2-(2-chloroacetamido) thiazole-4-yl) acetate were purchased from Merck (Germany). Various pesticides used for interference study, sodium borohydride ($NaBH_4$) and silver nitrate ($AgNO_3$), were acquired from Sigma Aldrich (USA). All the solutions were prepared in HPLC-grade solvents and DI water. All the sensing experiments were performed in DI water at room temperature.

All glassware was rigorously cleaned using 10% nitric acid, thoroughly rinsed with DI water, and then oven-dried to eliminate residual contaminants.

A Hanna Instruments HI2211 pH meter, equipped with a glass electrode and an Ag/AgCl reference electrode, was used to measure the pH values. UV-Visible absorbance spectra (300–800 nm) were obtained using a Shimadzu UV-1800 spectrophotometer (Japan) with measurements performed in quartz cuvettes having a 1 cm optical path length. The structural characterization of the synthesized compound was carried out using proton nuclear magnetic resonance (^{1}H-NMR) spectroscopy on a Bruker AV-300 spectrometer, with tetramethylsilane (TMS) serving as the internal reference. Spectral data were analyzed using Topspin software (version 3.6.1). The molecular mass of CT was identified using a JEOL-600H mass spectrometer. To examine the structural properties of CT-AgNPs, Powder X-ray diffraction (PXRD) analysis was conducted using a Bruker D8 Advance powder diffractometer. The instrument was operated with Cu-Kα radiation ($\lambda = 1.5406$ Å) as the X-ray source. The

measurements were taken at 40 kV and 25 mA, with scanning performed over a 2θ range of 20° to 90° at an incremental step size of 0.05° per min. FT-IR characterization was performed using a Bruker Vector 22 spectrometer, equipped with a deuterated triglycine sulfate (DTGS) detector. Spectral data were collected in the mid-IR range of 4000 to 500 cm^{-1} using the KBr pellet technique. Each spectrum was acquired at a resolution of 0.1 cm^{-1}, averaging ten scans per sample. The size distribution and surface charge (zeta potential) of CT-AgNPs were evaluated with a Nano-ZSP zeta sizer (Malvern Instruments) at 25 °C. Measurements were conducted at a fixed scattering angle of 90°, employing a disposable cuvette for particle sizing and a specialized zeta potential cell for analysis.

Topographical characterization of CT-AgNPs, both before and after the drug incorporation, was carried out using an Agilent 5500 Atomic Force Microscope (AFM) operating in tapping mode. The system was equipped with a triangular silicon nitride cantilever (Veeco MLCT-AUHW), featuring a spring constant of 0.1 N m^{-1}. For sample preparation, a drop of the NP suspension was placed onto a silicon wafer and allowed to dry at room temperature for 24 h. Surface morphology analysis *via* field emission scanning electron microscopy (FE-SEM) was performed using a Thermo Fisher Scientific Apero 2C LoVac SEM. Before imaging, the samples were gold-coated using a Quorum Technologies SC7620 mini sputter coater, with argon employed as the sputtering gas, resulting in an approximate coating thickness of 153 Å. Samples were prepared by drop-casting onto silicon wafers and dried under ambient conditions for 24 h before examination.

2.2 Synthesis of nanosensor

The synthesis procedure (Scheme S1-SI) and structural characterization of the Coumarin triazole are provided in the SI. The synthesized CT was thoroughly analyzed using various techniques, including fast atom bombardment mass spectrometry (FAB-MS) (Fig. S1-SI), and proton nuclear magnetic resonance (^{1}H-NMR) spectroscopy (Fig. S2-SI).

A 0.1 mM solution of CT was prepared by dissolving 2.17 mg of CT in 1 mL of DMSO, followed by dilution to a final volume of 50 mL with deionized (DI) water. Separately, aqueous solutions of 0.1 mM $AgNO_3$ and 5.0 mM $NaBH_4$ were prepared using DI water.

For the fabrication of nanoparticles, the CT, $AgNO_3$, and $NaBH_4$ solutions were mixed in a volumetric ratio of 1 : 10 : 0.1, respectively. Initially, a 0.1 mM $AgNO_3$ solution was transferred to a reaction flask and stirred magnetically at room temperature for 30 minutes. Subsequently, the 5.0 mM $NaBH_4$ solution was added dropwise using a micropipette over a period of 15 min under continuous stirring. The reaction mixture was then stirred for an additional 1 h to ensure complete reduction of Ag^+ ions.

The formation of CT-functionalized silver nanoparticles (CT-AgNPs) was confirmed by the appearance of a characteristic yellow coloration. Furthermore, the stability of the synthesized CT-AgNPs was systematically evaluated under various environmental conditions, including different pH levels, temperatures, and electrolyte concentrations. The resulting CT-AgNPs were characterized using a combination of spectroscopic and microscopic methods, including UV-Vis absorption spectroscopy, field emission scanning electron microscopy (FE-SEM), dynamic light scattering (DLS), atomic force microscopy (AFM), and powder X-ray diffraction (PXRD).

2.3 Detection procedure for CuOxy by colorimetric, smartphone, and paper-based sensors

2.3.1 Colorimetric method. The sensing ability of CT-AgNPs was evaluated using UV-Vis spectroscopy. Equal volumes of CT-AgNPs and different drug or pesticide samples were mixed, and changes in the color of the solution and corresponding absorption intensity were monitored. To assess the sensitivity of CT-AgNPs toward CuOxy, experiments were carried out using different concentrations of CuOxy. The detection limit (LoD) and quantification limit (LoQ) were determined based on the standard deviation of the blank and the slope of the calibration plot, applying the formulas: LoD = 3.3 × standard deviation/slope and LoQ = 10 × standard deviation/slope, respectively. Furthermore, selectivity studies were conducted to evaluate the response of CT-AgNPs to CuOxy in the presence of structurally or functionally similar drugs and pesticides.

2.3.2 Smartphone-based method in solution. A rapid and on-site method for detecting and quantifying CuOxy was developed using CT-AgNPs and a standard Android smartphone. Equal volumes of CT-AgNPs and CuOxy solutions ranging from 0.1 to 100 μM, were mixed in quartz cuvettes and placed under a fume hood. A smartphone, mounted on a tripod at a fixed distance of 20 cm, was used to capture images of the samples. These images were analyzed using the 'Color Meter' RGB color analysis app, freely available on the Android Play Store. A circular region of interest (ROI) of 150–200 pixels in diameter (~3–5 mm) was used for RGB value extraction to ensure consistent analysis. The values were extracted from three different points and averaged. The resulting data were employed to generate a calibration curve and assess the recovery rates of CuOxy in practical sample applications.

2.3.3 Paper-based assay. For the paper-based detection method, circular discs (0.5 cm in diameter) were punched from Whatman Grade 41 filter paper and affixed onto a hydrophobic paper backing. Each disc was treated with 10 μL of CT-AgNPs using a micropipette and left to air-dry. This application was repeated three times to ensure adequate nanoparticle deposition in the sensing zone. Once dried, 5 μL of CuOxy solution, at concentrations ranging from 0.1 to 100 μM, was added to each disc. The same procedure was applied for other analytes, but only at their maximum concentration. Colorimetric changes in the sensing zones were captured with a smartphone camera. The digital images were analyzed using FIJI software to generate color histograms and extract gray values. Mean gray intensity values from several regions on each disc were used to plot calibration curves and determine CuOxy concentrations in both standard solutions and real-world samples. Linear regression was applied using the equation $y = mx + c$ to correlate the observed intensity values with CuOxy levels across multiple test runs.

2.4 Detection of CuOxy in real samples

CT-AgNPs were employed for the detection of copper oxychloride (CuOxy) in six different real samples. Laboratory tap water, diluted two-fold with deionized (DI) water, was used according to the established protocol. In addition, four food matrices—guava, orange, turnip, and spinach—were procured from a local Metro vegetable market in Karachi. Environmental water samples were collected from the University of Karachi and the Sindh River.

For sample preparation, 20 g of each finely chopped fruit or vegetable was homogenized with 100 mL of DI water using a blender. The volume was then adjusted to 200 mL, followed by filtration through a 0.45 μm polytetrafluoroethylene (PTFE) syringe filter. Each real sample was spiked with CuOxy to obtain a final concentration of 100 μM.

The prepared samples were subsequently analyzed using three different colorimetric approaches, following the protocol described in Section 2.3, and the results were further validated by UPLC analysis. Each measurement was performed three times to ensure precision in quantification based on the previously established calibration curve.

Quantification was achieved using a calibration curve generated through linear regression analysis, and CuOxy recovery percentages were determined using eqn (1).

$$\text{Recovery}(\%) = \frac{\text{Calculated CuOxy concentration}}{\text{Total CuOxy concentration added}} \times 100 \quad (1)$$

2.5 UPLC analysis of CuOxy in different samples

The efficacy of the proposed CuOxy detection technique was validated using a variety of real samples and benchmarked against an ultra-performance liquid chromatography (UPLC) method.[17] Chromatographic separation was achieved on an Octadecyl Silica column (250 × 6.0 mm, JH08S04-2506WT) connected to a diode array detector (DAD). The absorbance at the wavelength of 254 nm was taken as a standard and used for quantification.

The mobile phase consisted of 30% Milli-Q water and 70% acetonitrile (ACN) delivered at a flow rate of 1.0 mL min^{-1}, with an injection volume of 1.0 μL. All analyses were conducted under isocratic conditions, and the column temperature was maintained at 30 °C.

Standard solutions of CuOxy were prepared in Milli-Q water, with the pH adjusted to acidic conditions using few drops of acetic acid. A calibration curve was constructed by plotting CuOxy concentrations in the range of 40–140 μM against the corresponding peak area values. Quantification of CuOxy in real water and food samples was carried out using this calibration curve. To evaluate the accuracy and recovery of the method, real samples were spiked with CuOxy at a concentration of 100 μM and subsequently analyzed by UPLC.

3 Results and discussion

Details regarding the synthesis and characterization of coumarin triazole (CT) are provided in the SI. The text herein focuses on the fabrication and analytical characterization of CT-AgNPs, along with their assessment as a colorimetric sensing platform.

3.1 Synthesis and characterization of CT-AgNPs

The synthesis of CT-AgNPs was accomplished through the chemical reduction method of $AgNO_3$ using $NaBH_4$ as a reducing agent, while coumarin triazole (CT) as a stabilizer, Scheme 1. Firstly, different concentrations of CT were used alongwith the 0.1 mM $AgNO_3$, and 0.1 mM provided the maximum absorption and was taken as the optimum for CT, Fig. S3-SI. To optimize the stability of CT-AgNPs, different volume ratios of 0.1 mM CT and 0.1 mM $AgNO_3$ solutions ranging from 1 : 3 to 1 : 15 were tested. Initially colorless CT solution turned yellow upon the formation of CT-AgNPs, as illustrated in Fig. 1A. The appearance of a vivid yellow color along with a pronounced SPR peak at 408 nm confirms the successful synthesis of CT-AgNPs, while CT had a characteristic absorption peak at 314 nm (Fig. 1A). The most intense SPR signal was recorded at a CT to $AgNO_3$ solutions ratio of 1 : 10, Fig. 1B. Therefore, the optimized ratio (1 : 10) was selected for the subsequent experiments involving CT-AgNPs.

The stability of CT-AgNPs was systematically investigated under various environmental parameters, as shown in Fig. 2. The stability of CT-AgNPs was monitored over 30 days under controlled storage conditions. The CT-AgNPs were kept at room temperature in sealed vials wrapped in aluminium foil to prevent light exposure. As shown in Fig. 2A, the SPR peak at ~420 nm remained sharp and unchanged throughout the study, with no noticeable peak shift or decrease in intensity. This indicates that the CT-AgNPs maintained excellent colloidal stability with no significant aggregation or degradation under these storage conditions. Elevated electrolyte concentrations frequently promote nanoparticle aggregation.[36] CT-AgNPs were exposed to different NaCl concentrations from 0.1 mM to 1000 mM to evaluate ionic strength tolerance. A noticeable decrease in SPR intensity and red shift at higher salt concentrations (250 mM) indicated partial aggregation, suggesting reduced stability under strong ionic conditions,[59] Fig. 2B. However, the CT-AgNPs remain quite stable under practical electrolyte concentrations of real samples. In addition, the thermal stability of CT-AgNPs was evaluated by subjecting the CT-AgNPs solution to a boiling temperature (100 °C). An increase in absorbance intensity was observed upon heating, indicating that the CT-AgNPs retained their stability after high-temperature treatment (Fig. 2C). The pH of the synthesized CT-AgNPs was 7. The stability of CT-AgNPs was further assessed across a pH range from 1 to 12. The CT-AgNPs maintained stability in the pH range of 4–10, whereas extreme acidic and basic conditions led to broadened and diminished SPR bands, indicating aggregation (Fig. 2D). As a result, pH 7 was selected for subsequent experimental procedures because it corresponds to the native pH of the synthesized CT-AgNPs, maintains nanoparticle stability within the pH window of 4–10, and matches the pH of real environmental samples. These findings confirm the suitability of CT-AgNPs for applications under physiological and moderately varied environmental conditions.

The average size, surface charge, and surface morphology of CT-AgNPs were investigated using DLS, AFM, and SEM. The DLS data revealed that the average particle size of CT-AgNPs was

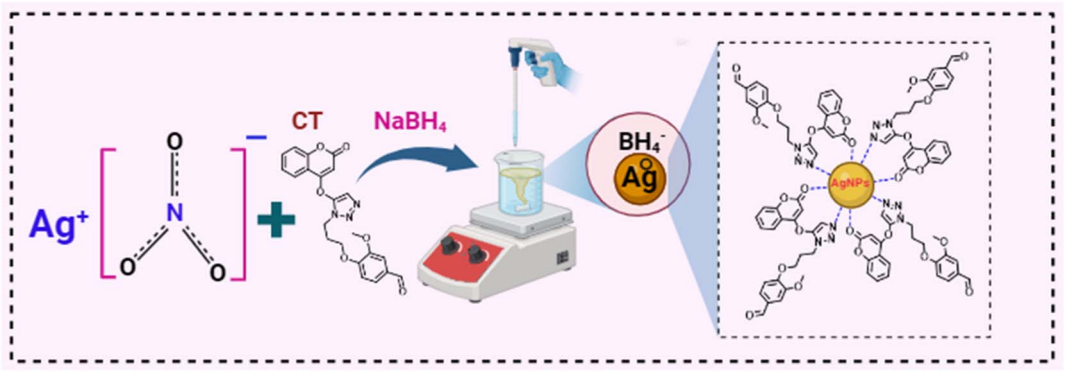

Scheme 1 Schematic representation for the synthesis of CT-AgNPs.

found to be 40.89 nm with a polydispersity index of 0.38, Fig. 3A. Additionally, zeta potential measurements of CT-AgNPs were found to be −28.7 mV, which shows the excellent stability of AgNPs (Fig. 3B). Moreover, the results obtained from DLS were further endorsed by AFM and SEM. The AFM topographical image a show a spherical morphology of CT-AgNPs, Fig. 3C and E. Fig. 3D depicts the histogram as obtained by AFM that revealed the average size of 34.8 nm. FE-SEM analysis demonstrated that the average particle size of CT-AgNPs was 38 nm with well-defined spherical morphology (Fig. 3F). The size of the CT-AgNPs predominantly remains within range of 30–40 nm. PXRD analysis was conducted to investigate the crystalline nature of silver within the CT-AgNPs. The resulting diffraction pattern displayed Bragg reflections at 2θ angles of 39.04°, 48.1°, 67.3°, and 77.2°, which are indicative of the (111), (200), (220), and (311) crystallographic planes, respectively, Fig. 3G.[60] The diffraction pattern confirms that the AgNPs possess a face-centered cubic (fcc) crystal structure. Additionally, the obtained XRD results are in good agreement with previously reported data for silver nanoparticles.[61,62]

3.2 CT-AgNPs as a colorimetric sensor

In this study, the influence of the addition of various drugs and pesticides/fungicides on the SPR band behavior of CT-AgNPs was evaluated. Twelve structurally diverse pesticides/fungicides, namely isoproturon, chlorothalonil, abamectin, propanil, trifluralin, urea, imidacloprid, diammonium phosphate (DAP), cymoxanil, ammonium sulfate, emamectin, and deconil, were introduced into the CT-AgNPs solution. The addition of these compounds produced no noticeable color alteration, indicating absence of any interaction with the CT-AgNPs. In contrast, introducing CuOxy to the CT-AgNPs solution led to a prompt visual change from pale yellow to light pink. This unique interaction was confirmed through UV-Vis spectroscopic analysis, where all other analytes caused negligible variations in the SPR band, while CuOxy significantly decreased the absorbance intensity and induced a bathochromic (red) shift, with the SPR peak moving to approximately 545 nm and becoming broader, Fig. 4A. The inset shows the color change in CT-AgNPs after the introduction of CuOxy in them. These findings strongly suggest that the CT-AgNPs

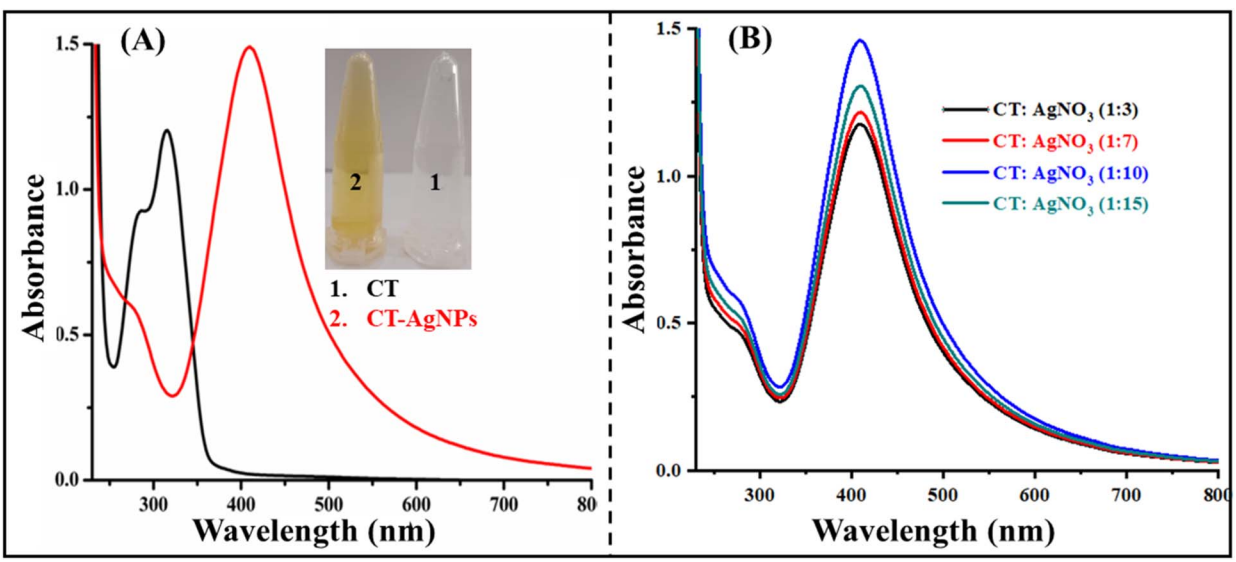

Fig. 1 (A) UV-Visible spectra of CT and CT-AgNPs (1–10); (B) optimization of the ratio CT and $AgNO_3$ for CT-AgNPs synthesis through UV-Visible analysis.

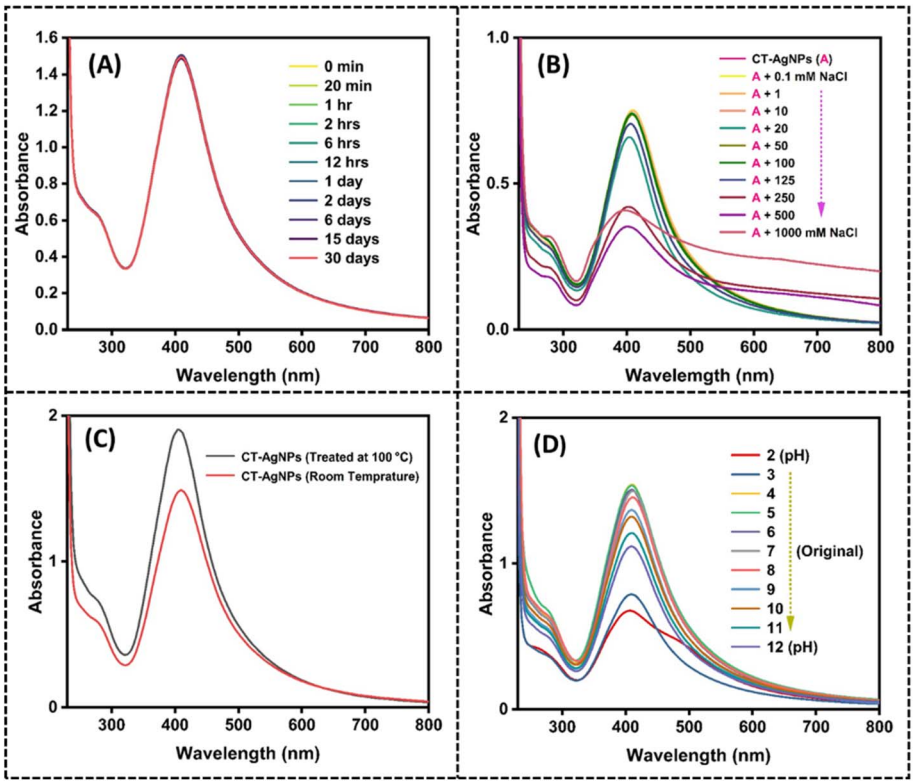

Fig. 2 Stability of CT-AgNPs through UV-Visible analysis as a function of (A) storage time, (B) ionic strength, (C) temperature, (D) pH.

exhibit selective binding and specific optical response only to CuOxy, establishing their potential as a targeted colorimetric sensor.

A rapid and on-site method for detecting and quantifying CuOxy was implemented using a standard Android smartphone. CT-AgNPs were placed in a transparent Eppendorf and positioned inside a fume hood under consistent LED lighting, Fig. 4C. To evaluate the selectivity of the CT-AgNPs-based detection system, 100 μM solutions of the previously mentioned analytes were introduced individually, and any resulting color changes were monitored. Digital images of each sample were captured using the smartphone camera after analyte addition. A noticeable color change in the CT-AgNPs was observed exclusively upon the addition of CuOxy, while other analytes produced negligible effects. Subsequently, the RGB intensities of the solutions were measured using a smartphone color analysis application. A bar graph was generated based on the red-to-green (R/G) ratios of CT-AgNPs before and after analyte addition. The R/G ratio remained approximately 1.75 for all analytes except CuOxy, which exhibited a decrease to 0.6, Fig. 4B.

In addition, a paper-based colorimetric sensor incorporating CT-AgNPs was fabricated and integrated with a smartphone for visual detection. Specific zones on the sensor paper were allocated to different analytes at a fixed concentration of 100 μM. No noticeable color alteration was observed in any of the zones except for the one containing CuOxy, which changed from yellow to a light pink color. This visible shift was captured using a smartphone camera. The resulting images were analyzed using FIJI software to assess color histograms and calculate gray values. The initial mean gray value of the CT-AgNPs was recorded as 128. Following the application of various analytes, no significant deviation in this value was detected. However, upon exposure to CuOxy, the mean grey value increased to 158, highlighting the system's sensitivity and specificity. This confirms the sensor's effectiveness for CuOxy detection, Fig. 4D and E. It is pertinent to mention here that the smartphone/paper-based sensor operates as a single-use device, similar to pH indicator strips; therefore, reusing the same strip for repeated measurements is not feasible. Reproducibility was evaluated by performing the assay in triplicate using freshly prepared strips, and the results are presented with error bars to demonstrate measurement consistency.

The changes in the average size, surface charge, and surface morphology of CT-AgNPs after the addition of CuOxy were evaluated using the aforementioned techniques. DLS revealed an increase in the size of CT-AgNPs to 215 nm upon CuOxy incorporation, Fig. 5A. This increase was accompanied by a minor rise in the polydispersity index from 0.38 to 0.42, suggesting a broader particle size distribution and supporting the aggregation behavior. Additionally, a shift in zeta potential from −28.7 mV to −19.6 mV was observed after CuOxy exposure, Fig. 5B, indicating reduced colloidal stability. Furthermore, the observations gathered from DLS were confirmed by AFM and FE-SEM analyses, which also showed an increase in particle size, Fig. 5C and D.

FT-IR spectroscopy was used to examine the functional group interactions that stabilize AgNPs with CT and their

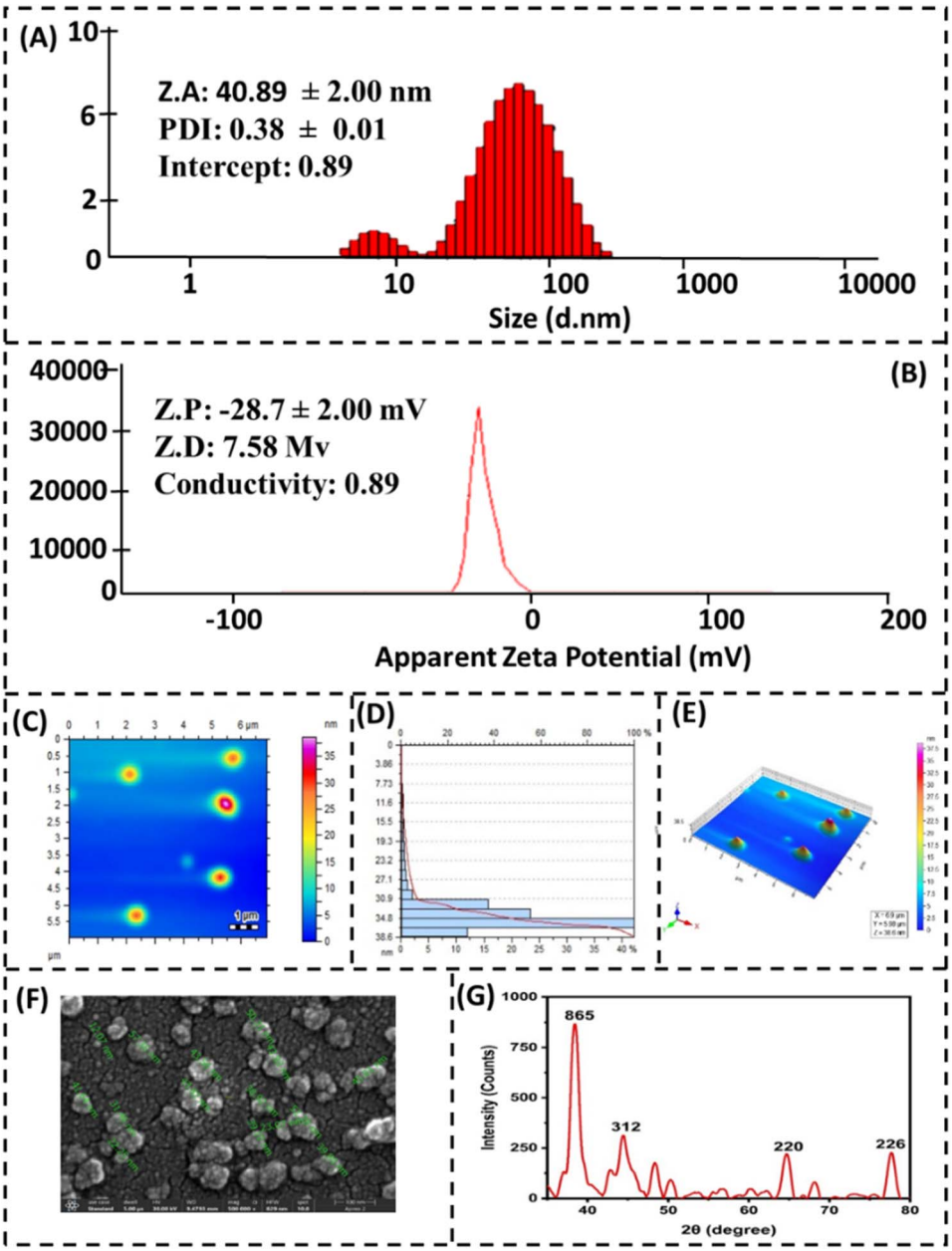

Fig. 3 Characterization of CT-AgNPs, (A) zeta size, (B) zeta potential, (C) AFM, (D) histogram obtained by AFM, (E) three dimensional image by AFM, (F) FE-SEM, (G) XRD.

response to CuOxy (Fig. 6). The FT-IR spectrum of pure CT shows a prominent absorption band at 1730 cm^{-1}, reflecting the stretching vibration of the carbonyl (–C═O) group in the coumarin part. Additionally, several bands in the 1300–1000 cm^{-1} range are assigned to C–O and C–N stretching vibrations, characteristic of the coumarin triazole backbone. When CT-AgNPs form, notable spectral changes occur. The intensity of the carbonyl band at 1730 cm^{-1} decreases substantially, and modifications are also seen in the C–O and C–N stretching bands in the 1300–1000 cm^{-1} region. These observations reveal that the carbonyl, ether, and amine groups of CT are directly involved in binding and capping AgNPs, confirming their role in stabilising the nanoparticles. The FT-IR spectrum of CuOxy shows characteristic vibrational features, while in the CT-AgNPs/CuOxy composite, a broad absorption band around 3400 cm^{-1} becomes evident. This band is linked to O–H stretching vibrations, indicating hydrogen bonding between CuOxy and surface-bound CT ligands. Notably, the band at 1631 cm^{-1}, related to AgNP formation, remains unchanged in both the spectra of CT-AgNPs and the CT-AgNPs/CuOxy complex. This suggests that CuOxy does not directly interact with the AgNP core; instead, it interacts mainly through the terminal functional groups of the CT ligands attached to the nanoparticle surface. These ligand-mediated interactions maintain the structural integrity of the AgNPs and facilitate effective recognition and sensing of CuOxy. Based on these FT-IR findings, a plausible mechanism for the CuOxy detection is proposed and depicted in Scheme 2.

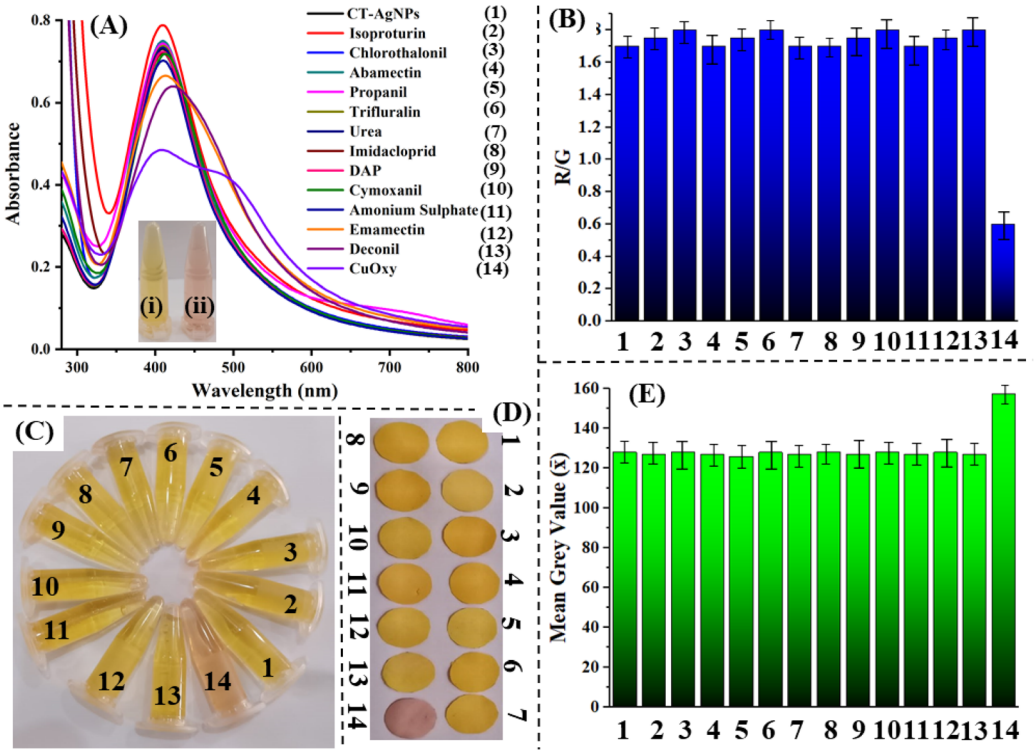

Fig. 4 (A) UV-Visible spectra of CT-AgNPs obtained upon the addition of a 100 μM of various drug solutions (The color change induced by the addition of CuOxy is depicted in the inset); (B) bar diagram for smartphone-based sensor showing *R*/*G* of CT-AgNPs + analytes; (C) visual change in the CT-AgNPs containing vials after addition of CuOxy and other analytes; (D) visual change in the CT-AgNPs coated paper after addition of CuOxy and other analytes; (E) bar diagram for paper-based sensor showing mean grey value of CT-AgNPs + analytes on paper; the numbers (1–14) correspond to the sequence in the legend of part A of the figure.

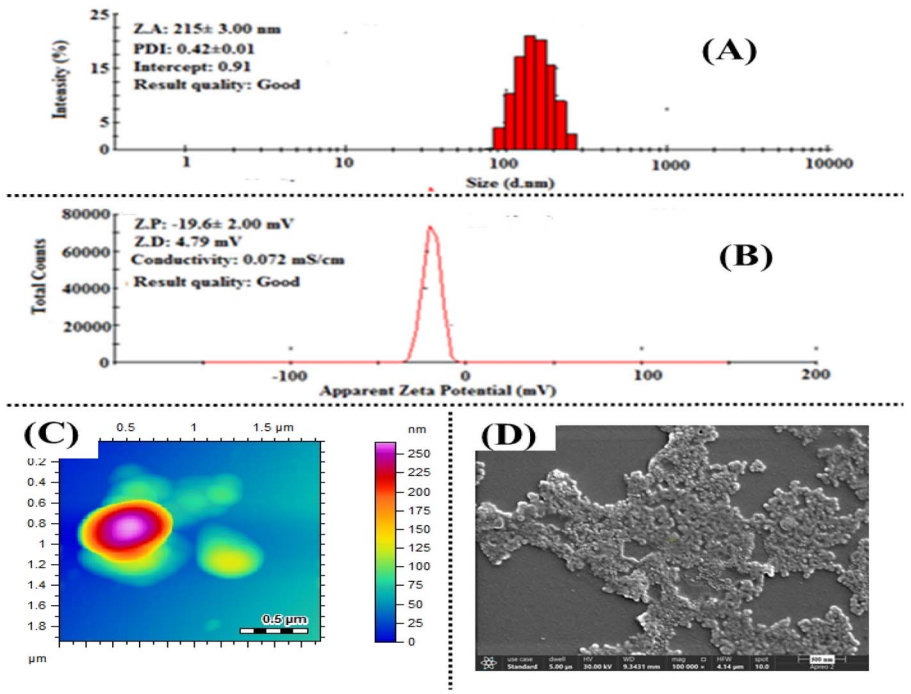

Fig. 5 Characterization of CT-AgNPs/CuOxy complex (A) average size through DLS, (B) zeta potential, (C) AFM, (D) FE-SEM.

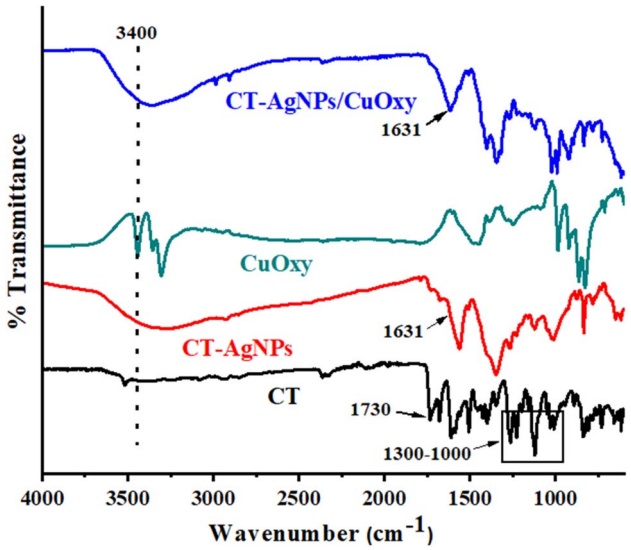

Fig. 6 FTIR spectra of CT, CT-AgNPs, CT-AgNPs/CuOxy.

3.3 Analytical figures of merit

The primary objective of this study is to synthesize a sensing material with selectivity, sensitivity, and specificity for CuOxy. The presence of CuOxy in CT-AgNPs caused a noticeable colour change, which was confirmed by a hypochromic shift and the band broadening in the SPR band (Fig. 4A). However, it is essential to assess the sensitivity of CT-AgNPs in the context of quantification. Hence, CT-AgNPs were exposed to different concentrations of CuOxy. When 0.1 μM CuOxy was added, the SPR band of CT-AgNPs underwent a slight hypochromic shift at 408 nm, which consistently decreased till the addition of 100 μM CuOxy, Fig. 7A. A direct linear correlation between the quantity of added CuOxy and the change in the intensity of the SPR band at 408 nm in the concentration range of 0.1 to 100 μM is established (Fig. 7B). The newly developed method for sensing CuOxy had a LOD of 0.007 μM and a LOQ of 0.023 μM, calculated as $3.3\sigma/S$ and $10\sigma/S$, respectively, in a linear dynamic range of 0.1–100 μM.[63]

The analytical performance of the PADs and smartphone-based CuOxy sensing devices developed using CT-AgNPs was also thoroughly investigated. The sensitivity of the proposed detection technique was assessed using a smartphone by varying the CuOxy concentration in the range of 0.1 to 100 μM in an Eppendorf containing CT-AgNPs solution (Fig. 7C, inset). At each concentration, images of the Eppendorf tubes were recorded and analyzed using a color-picking application. The corresponding *R*, *G*, and *B* values were extracted and transferred to a computer for linear fitting. Among the different parameters tested, the *R*/*G* ratio exhibited the best linear correlation with CuOxy concentration over the range of 0.1–100 μM, Fig. 7C. The corresponding LoD and LoQ were calculated to be 0.009 μM and 0.03 μM, respectively.

In addition, 5.0 μL of CuOxy solution with concentrations ranging from 0.1 to 100 μM was precisely applied to the detection zone of the paper-based sensor using a micropipette (Section 2.3.3). The subsequent color variation in the detection zone was documented with a smartphone camera. A clear trend was observed, as higher CuOxy concentrations produced a progressively lighter pink coloration. To quantitatively analyse this change, the captured images were processed in FIJI for colour histogram and grey value analysis. A calibration curve was plotted with the mean grey value as a function of CuOxy concentration, Fig. 7D. The visual changes in the detection zone as a function of added CuOxy concentration are shown in the Fig. 7D-inset. This confirms a strong correlation between mean gray value and CuOxy concentration, with a calculated LoD of 0.01 μM and LoQ of 0.033 μM.

The Bland–Altman plot was employed to evaluate the degree of agreement between two measurement methods. In this study, Bland–Altman analysis was applied to compare copper oxychloride concentrations determined by the spectrophotometric method with those obtained using two alternative approaches: a portable paper-based analytical device and a smartphone-based colorimetric method.

The results from the paper-based analytical device showed good agreement with the UV-Visible spectrophotometric reference method (Fig. S4A-SI). The mean difference (bias) between

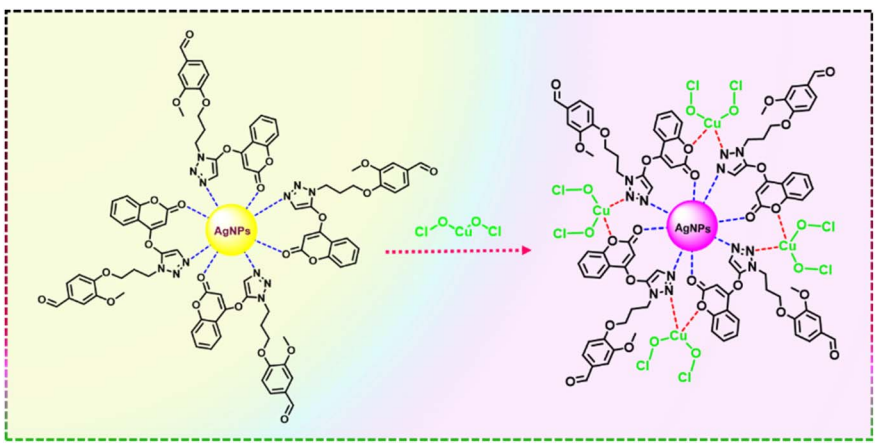

Scheme 2 Proposed sensing mechanism of CuOxy using CT-AgNPs.

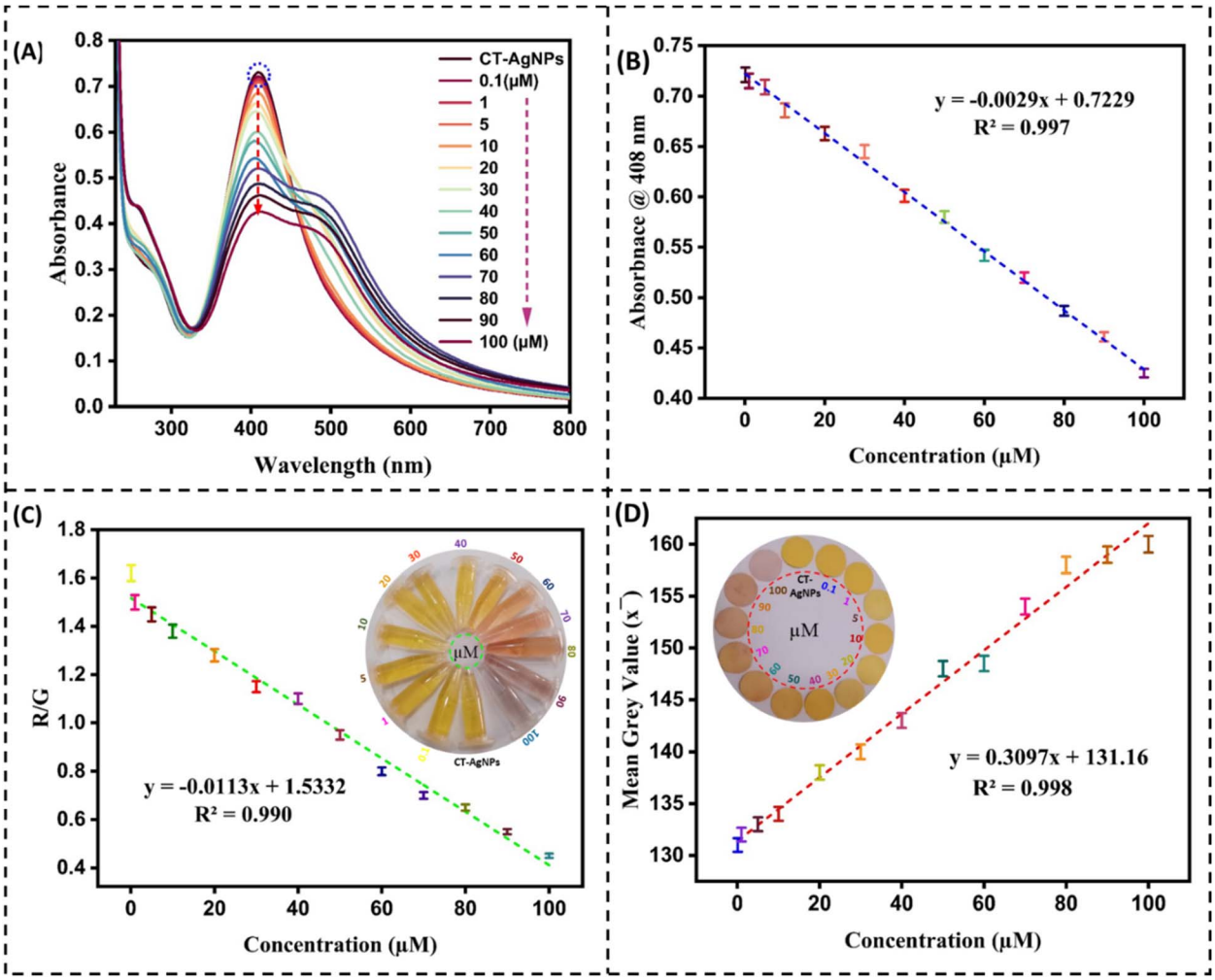

Fig. 7 Characterization of CT-AgNPs in response to varying concentrations of CuOxy (A) UV-Visible spectrphotometry, (B) calibration curve illustrating the correlation between CuOxy concentration and the absorbance at 408 nm, (C) CuOxy concentration as a function of the normalized intensity (*R*/*G*) though smartphone solution based analysis, (D) CuOxy concentration as a function of mean grey values using paper based sensor; corresponding digital images are shown in the inset of each part of the figure.

the two methods was −0.96 (pink line), indicating a slight underestimation of copper oxychloride concentration by the paper-based device relative to the reference method. Similarly, Bland–Altman analysis comparing the smartphone-based colorimetric method with the UV-Visible spectrophotometer (Fig. S4B-SI) revealed a mean bias of −0.291 (pink line), suggesting minimal systematic error between the test and reference methods.

In both Fig. S4A and S4AB-SI, the 95% limits of agreement (blue and green dotted lines) ranged from −9.69 to 7.72 and −8.97 to 8.39, respectively, indicating that the two alternative methods differed from the reference method by approximately ±8–9 concentration units across the measurement range. Overall, the Bland–Altman validation demonstrates that the developed paper-based analytical device and the smartphone-based colorimetric approach provide colorimetric detection performance comparable to that of the spectrophotometric method, supporting their suitability as reliable, low-cost alternatives for copper oxychloride quantification.

A key feature of any nanosensor is its ability to distinguish a target analyte even when other potentially interfering substances, such as similar pesticides or fungicides, are present. To assess the selectivity of the developed approach, a thorough series of experiments was conducted.[64] In this context, equal amounts of similar concentrations (70 μM) of other fungicides and pesticides, including isoproturon, chlorothalonil, abamectin, propanil, trifluralin, urea, imidacloprid, DAP, cymoxanil, ammonium sulphate, emamectin, and deconil, were introduced alongside CuOxy. The absorbance response of the sensor showed only minor deviations compared to the standard CuOxy detection, indicating its high specificity in the presence of potential interferents, Fig. 8. The recoveries of CuOxy in the presence of interfering compounds remained in a range of 98.13 to 104.72%, Table S1-SI. Furthermore, to determine the optimal ratio between CT-AgNPs and CuOxy, a Job's plot was constructed, revealing a 1 : 1 stoichiometric interaction (Fig. S5-SI). This analysis describes stoichiometric behaviour but does not imply a specific coordination structure

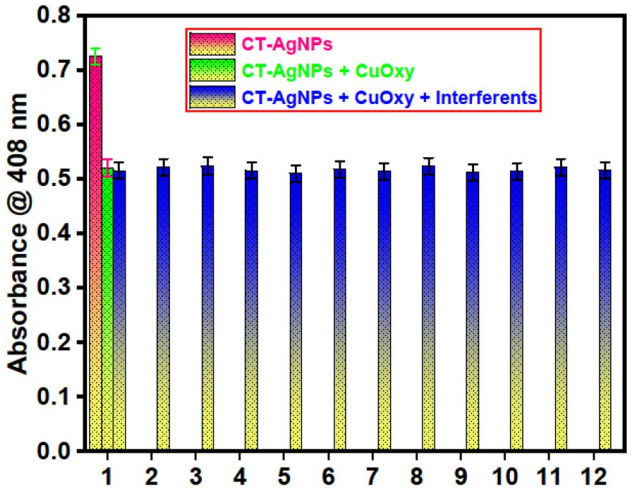

Fig. 8 Influence of different interfering species on the selectivity of CT-AgNPs towards CuOxy evaluated by UV-Vis spectrophotometry; 1. Isoproturin, 2. Chlorothalonil, 3. Abamectin, 4. Propanil, 5. Trifluralin, 6. Urea, 7. Imidacloprid, 8. DAP, 9. Cymoxanil, 10. Amonium Sulphate, 11. Emamectin, 12. Daconil.

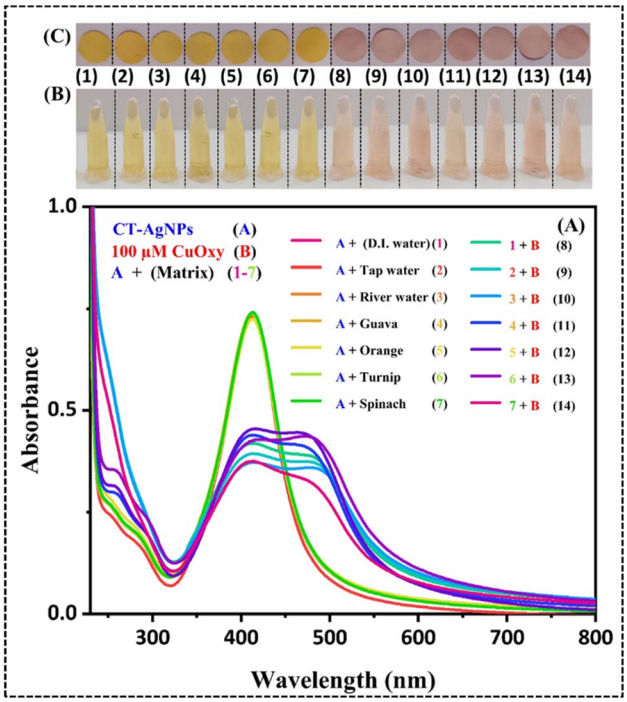

Fig. 9 The sensing capability of the CT-AgNPs-based sensor in tap water and river water, as well as in guava, orange, turnip, and spinach samples, evaluated using UV-Vis spectrophotometric method (A), visual changes in the color of solution in vial that is followed by analysis of *R*/*G* value (B), and visual changes in the color of detection zone on the paper that is followed by analysis of mean grey values (C).

at the molecular level. It should be noted that the reported 1 : 1 stoichiometric relationship reflects the experimentally optimized ratio that yielded the maximum colorimetric response under the present conditions. A more rigorous determination of binding constants and detailed molecular interaction mechanisms was beyond the scope of this study and will require further in-depth investigation using advanced physicochemical and spectroscopic approaches.

Initially, all experiments were conducted in DI water. To verify whether the CT-AgNPs-based CuOxy sensor is suitable for real-world applications, the same sensing method was applied to environmental water samples, including tap water (TW) and river water (RW), as well as food samples, such as guava, orange, turnip, and spinach (Fig. 9). The food samples show maximum absorption below 400 nm, thus not interfering with the UV-Vis peak of CT-AgNPs at 408 nm (Fig. S6-SI). Upon addition of CuOxy in different matrices making a final concentration of 100 µM and their addition to CT-AgNPs resulted in change of the typical yellow colour of CT-AgNPs to pink. This visible transformation was further confirmed by the characteristic hypochromic shift in the SPR band of CT-AgNPs, as shown in the UV-Vis spectra (Fig. 9A). The SPR band behaviour remained reasonably aligned with the standard calibration curve in all cases, validating the sensor's consistent performance in real samples, even in the presence of naturally occurring interferents.

In addition to the UV-Vis spectrohpotometric, smartphone-assisted solution-based and smartphone-assisted paper-based sensing platforms were also employed to detect CuOxy in the same real samples. The detection zone on the paper sensor and in the vial, after application of CuOxy-spiked water and food samples, showed a clear change in colour from yellow to pink in all matrices (Fig. 9B and C). These changes were captured using a smartphone, and the images were analysed using colourimetric tools to extract quantitative information. The results demonstrated excellent consistency with the standard analytical performance, with recoveries in a range of 93.41–113.66%, 94.97–108.13%, 95.94–112.85% for UV-Vis spectrophotometric, smartphone-assisted solution-based, and smartphone-assisted paper-based methods in the same order (Table S2-SI), thereby confirming the feasibility, reliability, and sensitivity of the CT-AgNPs-based UV-Vis, smartphone-based solution, and smartphone-based paper sensor for CuOxy detection in environmental and food samples. These results indicate that the nanoprobe is very specific for detecting CuOxy, and components in real water samples and food matrices do not interfere with the detection.

Moreover, the efficacy of the proposed CuOxy detection technique was also validated and benchmarked against a reported ultra-performance liquid chromatography (UPLC) method.[17] The method was developed using DI water as sample solvent having concentrations of CuOxy in a range of 40–140 µM, Fig. S7-SI. The calibration curve of the CuOxy concentration as a function of the absorption peak area at 2.8 mL is depicted in Fig. S8-SI. Lastly, the spiked samples analyzed by the developed methods in this study were analyzed by the reported UPLC method vis-à-vis. Fig. S9A-SI depicts the elugrams of blank matrices at the optimized UPLC conditions, while Fig. S9B-SI depcts the spiked real samples with 100 µM CuOxy chloride. The absence of a peak at 2.8 mL in all blank smaples confirm that CuOxy was not used in their production. The same samples

Table 1 Comparison of proposed and reported methods in terms of analytical figures of merit for copper oxychloride assay

Method	LDR	LDR (nM)[a]	LoD	LoD (nM)[a]	Samples	Remarks	Ref.
FIA	0.001 to 10 μg L^{-1}	4.68 × 10^{-3}–46.8	2.62 × 10^{-4} μg L^{-1}	1.23 × 10^{-3}	Peach, guava, banana, apple, and sapodilla	Expensive instrumentation, intricate preparation, and skilled operation	17
RP-HPLC-UV	10–50 mg L^{-1}	4.68 × 10^{7}–2.34 × 10^{8}	0.003 mg kg^{-1}	14	Coconut water	High-cost instrumentation, lengthy protocols	19
ETAAS	0.19–20 μg L^{-1}	0.88–9.3 × 10^{-8}	3.8 ng	1.78 ×10^{4}	Olive tree	High-cost instrumentation, lengthy protocols, and requires trained operators	21
LCMS/AAS	0.2 to 20 mg L^{-1}	1.1 × 10^{3}–1.1 × 10^{5}	0.07 mg L^{-1}	328	Grapes	High-cost instrumentation, lengthy protocols, expensive standards, tedious sample preparation, and optimization problems	22
CT-AgNPs	0.1–100 μM	100–100000	0.007 0.009 0.01	7.0, 9.0, and 10	Tap water, river water, guava, orange, spinach, and turnip	Economical, simple, no sample pre-treatment, highly selective and sensitive, enables on-site visual and quantitative water analysis *via* paper- and smartphone-based methods	This study

[a] Converted to nanomolar for better comparison.

were spiked with 100 μM of CuOxy and analyzed by the UPLC method, as was done for the developed sensor methods in this study. The peak at 2.8 mL clearly shows the presence of CuoXY compared to blank samples. The recoveries of the CuOxy in real samples by this method remained in a range of 90.24–106.95%, Table S2-SI. The UPLC results validate the outcome of different approaches of the sensors developed in this study.

The comparative analysis of the current study with previously reported CuOxy sensors is presented in Table 1, which clearly highlights that the detection limit achieved by the current sensor is significantly lower than most existing methods.

4 Conclusions

In this study, CT-capped silver nanoparticles (CT-AgNPs) were synthesized and utilized as an efficient colourimetric sensor for the quick and sensitive detection of copper oxychloride (CuOxy). The developed sensor demonstrated a remarkably low limit of detection (LoD) of 0.007 μM and a limit of quantification (LoQ) of 0.023 μM, with a linear dynamic range (LDR) spanning from 0.1 to 100 μM under optimized conditions. Integration of the sensor with smartphone-based analysis enabled in-solution detection, and it was also embedded into paper-based analytical platforms for on-the-spot applications. The LoD and LoQ for smartphone in-solution analysis were 0.009 μM and 0.03 μM, respectively. Similarly, the LoD and LoQ of the paper-based assay were 0.01 μM and 0.03 μM. The CT-AgNPs sensor exhibited high selectivity for CuOxy even in the presence of various other pesticides and fungicides. To validate its real-world applicability, the sensor was tested in actual water samples and food samples, confirming its capability as a rapid, on-site, non-destructive, and reliable detection system for CuOxy in environmental settings.

Conflicts of interest

Authors declare no conflicting financial interests.

Data availability

The data that support the findings of this study are available from the corresponding author upon reasonable request.

Supplementary information (SI) is available. See DOI: https://doi.org/10.1039/d5ra08077k.

Acknowledgements

The authors received no specific financial support for research, authorship, or publication of this particular article.

References

1 D.-P. Häder, A. T. Banaszak, V. E. Villafañe, M. A. Narvarte, R. A. González and E. W. Helbling, *Sci. Total Environ.*, 2020, **713**, 136586.

2 D. Ghosh, S. Chaudhary, S. Sarkar and P. Singh, *Water Resour. Manage. Rural Dev*, 2024, 15–28.
3 I. Ali, S. Khan, Z. Ali Shah, F. Ahmed, I. Shah, A. Hameed, R. Ullah and M. Raza Shah, *Chem. Select.*, 2024, **9**, e202304484.
4 N. Morin-Crini, E. Lichtfouse, G. Liu, V. Balaram, A. R. L. Ribeiro, Z. Lu, F. Stock, E. Carmona, M. R. Teixeira and L. A. Picos-Corrales, *Environ. Chem. Lett.*, 2022, **20**, 2311–2338.
5 R. K. Mishra, S. S. Mentha, Y. Misra and N. Dwivedi, *Water-Energy Nexus*, 2023, **6**, 74–95.
6 M. Syafrudin, R. A. Kristanti, A. Yuniarto, T. Hadibarata, J. Rhee, W. A. Al-Onazi, T. S. Algarni, A. H. Almarri and A. M. Al-Mohaimeed, *Int. J. Environ. Res. Public Health.*, 2021, **18**, 468.
7 C. Panis, L. Z. P. Candiotto, S. C. Gaboardi, S. Gurzenda, J. Cruz, M. Castro and B. Lemos, *Environ. Int.*, 2022, **165**, 107321.
8 Z. Zhang, X. Yan, K. C. Jones, C. Jiao, C. Sun, Y. Liu, Y. Zhu, Q. Zhang, L. Zhai and Z. Shen, *npj Clean Water*, 2022, **5**, 59.
9 R. Painuli, S. Raghav, P. C. Jha, M. Athar and D. Kumar, *Inorg. Nano-Metal Chem.*, 2023, **53**, 239–256.
10 P. Kudsk, L. N. Jørgensen and J. E. Ørum, *Land Use Policy*, 2018, **70**, 384–393.
11 C. Corvalan, S. Hales, A. J. McMichael and C. Butler, *Ecosystems and Human Well-Being: Health Synthesis*, World health organization, 2005.
12 L. Rani, K. Thapa, N. Kanojia, N. Sharma, S. Singh, A. S. Grewal, A. L. Srivastav and J. Kaushal, *J. Clean. Prod.*, 2021, **283**, 124657.
13 S. Kumari, K. S. Sharma, M. Nemiwal, S. Khan and D. Kumar, *Int. J. Phytorem.*, 2022, **24**, 808–821.
14 N. A. Rajpurohit, K. Bhakar, M. Nemiwal and D. Kumar, *Arabian J. Geosci.*, 2022, **15**, 1–16.
15 P. Marriage, W. Saidak and F. Von Stryk, *Weed Res.*, 1975, **15**, 373–379.
16 D. J. Lapworth, B. Lopez, V. Laabs, R. Kozel, R. Wolter, R. Ward, E. V. Amelin, T. Besien, J. Claessens and F. Delloye, *Environ. Res. Lett.*, 2019, **14**, 035004.
17 K. U. N. Jaffar, K. A. U. Rehman, A. Muhammad, U. Sami, K. Naqeebullah, H. Abdul, A. Manzoor and S. Afsar, *J. Liq. Chromatogr. Relat. Technol.*, 2025, **48**, 37–47.
18 H. C. Menezes, B. P. Paulo, M. J. N. Paiva and Z. L. Cardeal, *J. Anal. Methods Chem.*, 2016, **2016**, 7058709.
19 R. Paranthaman and S. Kumaravel, *J. Chromatogr. Sep. Tech.*, 2013, **4**, 1000208.
20 H. Karasali, K. M. Kasiotis, K. Machera and A. Ambrus, *J. Agric. Food Chem.*, 2014, **62**, 11347–11352.
21 M. E. Soares, J. A. Pereira and M. L. Bastos, *J. Agric. Food Chem.*, 2006, **54**, 3923–3928.
22 Y. Verma, T. Bharat, K. Pratap, H. Sandip and Tp Shabeer, *J. Environ. Sci. Health, Part B*, 2022, **57**, 670–679.
23 C. Yuan, L. Sun, Z. Wang, X. Hong, H. He, X. Lu and Z. Chen, *Langmuir*, 2025, **41**, 11046–11055.
24 M. Yuan, X. Yuan, Y. Jin, Y. Shi, Z. Zou and X. Xiong, *Microchem. J.*, 2025, **210**, 112969.
25 J. Huang, H. Zhao, X. Chen, T. Lin, L. Hou and S. Zhao, *Spectrochim. Acta, Part A*, 2025, **333**, 125894.
26 M. Mascini, S. Gaggiotti, F. Della Pelle, J. Wang, J. M. Pingarrón and D. Compagnone, *Biosens. Bioelectron.*, 2019, **123**, 124–130.
27 A. Masri, A. Anwar, D. Ahmed, R. B. Siddiqui, M. Raza Shah and N. A. Khan, *Antibiotics*, 2018, **7**, 100.
28 S. Panicker, A. Prabhu, B. Sundarrajan, B. P. Quadros and N. K. Mani, *Anal. Methods*, 2024, **16**, 6264–6270.
29 S. Sarwar, D. A. Raja, D. Hussain, M. R. Shah and M. I. Malik, in *Handbook of Nanomaterials*, ed. M. I. Malik, D. Hussain, M. R. Shah and D.-S. Guo, Elsevier, vol. 1, 2024, pp. 1–26, DOI: 10.1016/B978-0-323-95511-9.00012-3.
30 X. Fu, H. Lin, J. Qi, F. Li, Y. Chen, B. Li and L. Chen, *Sens. Actuators, B*, 2022, **362**, 131830.
31 J. Khatoon, M. R. Shah, M. I. Malik, I. A. T. Khan, S. Khurshid and R. Naz, *RSC Adv.*, 2019, **9**, 2978–2996.
32 N. ul Ain, Z. Aslam, M. Yousuf, W. A. Waseem, S. Bano, I. Anis, F. Ahmed, S. Faizi, M. I. Malik and M. R. Shah, *New J. Chem.*, 2019, **43**, 1972–1979.
33 D. A. Raja, M. R. Shah and M. I. Malik, *Anal. Chim. Acta*, 2022, **1223**, 340216.
34 D. A. Raja, S. G. Musharraf, M. R. Shah, A. Jabbar, M. I. Bhanger and M. I. Malik, *J. Ind. Eng. Chem.*, 2020, **87**, 180–186.
35 D. A. Raja, F. Munir, M. R. Shah, M. I. Bhanger and M. I. Malik, *R. Soc. Open Sci.*, 2021, **8**, 210185.
36 D. A. Raja, S. Rahim, M. R. Shah, M. I. Bhanger and M. I. Malik, *J. Mol. Liq.*, 2023, **372**, 121200.
37 A. Aijaz, D. A. Raja, F.-A. Khan, J. Barek and M. I. Malik, *Chemosensors*, 2023, **11**, 91.
38 A. Talha, D. A. Raja, D. Hussain and M. I. Malik, *Microchim. Acta*, 2024, **191**, 164.
39 D. A. Raja, A. Bano, M. Zehra, I. Vohra, S. Ahmed, A. Ahmed, M. I. Bhanger and M. I. Malik, *Colloids Surf., A*, 2024, **695**, 134264.
40 I. Ali, D. A. Raja, F. Ahmed, M. Fazal, A. Hameed, M. R. Shah and M. I. Malik, *J. Mol. Struct.*, 2024, **1315**, 138971.
41 N. Iqbal, B. Amber, R. D. Asif, R. Ali, I. Rabia, A. Rafia, S. Imran, A. Ayaz, M. S. Ghulam and M. I. and Malik, *Drug Dev. Ind. Pharm.*, 2024, **50**, 789–800.
42 M. Z. Malik, D. A. Raja, D. Hussain and M. I. Malik, *J. Environ. Chem. Eng.*, 2024, **12**, 113626.
43 S. K. Sonawane, A. Ahmad and S. Chinnathambi, *ACS Omega*, 2019, **4**, 12833–12840.
44 O. Bulut and M. D. Yilmaz, *ACS Appl. Nano Mater.*, 2022, **5**, 13761–13767.
45 M. I. Malik, B. Trathnigg and C. O. Kappe, *J. Chromatogr., A*, 2009, **1216**, 1167–1173.
46 R. Abdul-Karim, A. Hameed and M. I. Malik, *Eur. Polym. J.*, 2018, **105**, 95–106.
47 I. Ali, S. Khan, C. A. T. Toloza, Z. A. Shah, Z. Iqbal, R. Ullah and M. R. Shah, *J. Mol. Str.*, 2025, **1323**, 140587.
48 T. Qadri, S. Khan, I. Begum, S. Ahmed, Z. A. Shah, I. Ali, F. Ahmed, M. Hussain, Z. Hussain, S. Rahim and M. R. Shah, *J. Mol. Str.*, 2022, **1267**, 133589.

49 S. Khan, I. Ali, A. Ali, C. A. T. Toloza, N. Ahmad and M. R. Shah, *Opt. Mater.*, 2025, **164**, 117088.
50 Y. Manmana, S. Kinugasa, Y. Hiruta and D. Citterio, *Anal. Chem.*, 2025, **97**, 1500–1506.
51 H. Wang, L. Dong, G. Ma, S. Qiu, G. Shan, L. Zhao, Y. Sun, A. Cui, R. Zhang and X. Liu, *Anal. Chim. Acta*, 2025, **1336**, 343489.
52 D. Lin, B. Li, L. Fu, J. Qi, C. Xia, Y. Zhang, J. Chen, J. Choo and L. Chen, *Microsyst. Nanoeng.*, 2022, **8**, 53.
53 B. Chettri, R. S. Fernandes, S. Jha and N. Dey, *Spectrochim. Acta, Part A Mol. Biomol. Spectrosc.*, 2024, **308**, 123620.
54 A. S. Mohitkar, N. Dey and S. Jayanty, *RSC Sustain.*, 2024, **2**, 3946–3958.
55 A. Pal and N. Dey, *J. Fluoresc.*, 2025, **35**, 1335–1344.
56 U. Salma, M. Z. Alam, S. Ahmad, M. Mohasin and S. A. Khan, *Inorg. Chim. Acta*, 2025, **582**, 122600.
57 A. L. Mohamed, A. G. Hassabo, S. Shaarawy and A. Hebeish, *Carbohydr. Polym.*, 2017, **178**, 251–259.
58 B. M. Geetha, K. N. Brinda, G. Achar, J. G. Małecki, M. Alwarsamy, V. S. Betageri and S. Budagumpi, *J. Mol. Liq.*, 2020, **301**, 112352.
59 S. Rahim, S. Perveen, S. Ahmed, M. R. Shah and M. I. Malik, *R. Soc. Open Sci.*, 2020, **7**, 201097.
60 Y. Meng, *Nanomaterials*, 2015, **5**, 1124–1135.
61 M. Sadeghi-Kiakhani, E. Hashemi, M.-M. Norouzi, P. Soleimani and V. Babaahmadi, *J. Ind. Eng. Chem.*, 2025, **145**, 732–744.
62 C. A. Z. Souto, F. G. de Souza, K. Pal, J. T. de Seixas Filho, H. K. Toma, N. Asthana, A. A. Khan and S. Fatima, *J. Mol. Struct.*, 2025, **1321**, 139961.
63 C. Saenjum, N. Pattapong, T. Aunsakol, T. Pattananandecha, S. Apichai, H. Murakami, K. Grudpan and N. Teshima, *J. Food Compos. Anal.*, 2022, **105**, 104215.
64 S.-J. Kim, S.-J. Choi, J.-S. Jang, H.-J. Cho and I.-D. Kim, *Acc. Chem. Res.*, 2017, **50**, 1587–1596.